age, leading to a huge amount of economic loss. Besides, the invalid spacecraft occupy valuable space orbits, which is a waste of orbit resources. It is a promising strategy to capture the invalid spacecraft and then fix or refuel it on-orbit, which is called on-orbit maintenance or on-orbit servicing (OOS) [Stoll, Letschnik, Walter et al. (2009); Badawy and McInnes (2008); Saleh, Lamassoure, Hastings et al. (2003)]. The OOS for the invalid satellite is regarded as one of the most difficult space missions, due to (i) the invalid satellite is a non-cooperative target, which cannot provide its own state information to the servicing spacecraft and (ii) the target does not have a specialized docking mechanism, so its engine nozzle is usually selected as a capture component. Both the above facts make the impact between the servicing spacecraft and the target inevitable. During the past decade, more attentions have been paid to vibration suppression of the spacecraft especially suffering an impact after capturing the target. The post-capture vibration control of the combined spacecraft system is highly required.

According to the differences of vibration sources, post-capture vibrations of spacecraft can be generally classified into two types: the high frequency periodic excitation and the impact excitation. The former arises from the moving payloads mounted on the target, such as the reaction flywheel and the driving mechanism of solar panel. The latter comes from collisions between the servicing satellite and the target [Xavier, Sun-Wook, Michel et al. (1997)]. In the mission of capturing a non-cooperative target, the impact between the servicing spacecraft and the target may be significantly strong. Unfortunately, until the work by Dai et al. [Dai, Jing, Wang et al. (2018); Dai, Jing, Sun et al. (2018)], almost all the existing studies use the rigidly connected system to model the combined spacecraft system, which means that the servicing satellite and the target are considered to be rigidly connected without relative motion. This model is oversimplified for the non-cooperative capture mission. Neglecting the mutual impact would make the post-capture spacecraft unstable or even tumbling. Therefore, a novel "loose-connection" pattern was proposed by Dai et al. [Dai, Jing, Wang et al. (2018)] to describe the sudden impact between the servicing satellite and the target at the moment of touch.

Normally, passive control as the most mature technology is widely applied for on-orbit vibration isolation missions. Various passive systems in the present literatures can easily achieve good vibration isolation performance, which is known for high reliability, easy implementation and low development cost. The SMD isolator [Park (1967)] is regarded as a typical passive control strategy for vibration isolation. However, increasing the linear damping of the SMD system can decrease the transmissibility on the region of natural frequency and deteriorate the vibration isolation performance at high frequency range. And there still exists some problems in the passive control methods, including poor instability, low loading capability and potential bifurcation effects.

To improve the vibration isolation performance, semi-active methods are always used to suppress vibrations of system whose stiffness and damping can be modified under different conditions. They can achieve excellent isolation performance for low frequency vibrations with sufficient loading capacity and robustness. Many efficient semi-active methods including using magnetorheological fluids [Oh (2004)] and some smart materials [Clark (2000)] have been widely studied before. Actually, semi-active isolation is a passive

control method in essence, which still has limitations of passive isoaltion. To overcome the limitations, active vibration control mechanism including drivers, actuators and sensors is proposed, which can achieve excellent performance for low frequency vibration with efficient loading capacity and robustness simultaneously. For instance, an active vibration controller based on the coupling dynamics was designed in Yuan et al. [Yuan, Liu and Qi (2017)] and applied to the maneuvering spacecraft, which can suppress the vibrations of the flexible structures efficiently. The active control of electric field for suppressing vibration of the moving beam was proposed and verified to be very effective in Lin [Lin (2009)]. Optimal performance of MFC (macro fibre composites) actuators and sensors for vibration suppression of rotating composite beams was studied in Vadiraja et al. [Vadiraja and Sahasrabudhe (2008)] and some quasi-optimal control algorithms have also been proposed by Abakumov et al. [Abakumov and Miatov (2006)]. To achieve higher reliability and obtain better performance, the hybrid passive/active vibration isolation methods can be used commonly, which has the strengths of both passive and active isolators.

Recently, a kind of passive vibration isolation structure referred to as X-shape structure was designed to isolate vibrations by Sun et al. [Sun and Jing (2016, 2015); Liu, Jing and Chen (2016); Liu, Jing and Li (2015)]. This kind of structure can provide nonlinear damping and nonlinear stiffness by geometrical relations of the rods, rotation joints and springs. It can achieve very low resonance frequency and large displacement motion, but simultaneously maintain a good and designable loading capacity without the stability issue. Besides, it can be easily assembled and flexibly implemented in practical applications. Based on the above superiority, Dai et al. [Dai, Jing, Wang et al. (2018)] first combined the X-shape structure with robotic arms tactfully to suppress vibrations of a free-floating spacecraft subjected to periodic or impulsive excitations, which can be encountered during performing the on-orbit servicing missions. The effects of structure parameters on the isolation performance for the satellite platform and the capture mechanism have been studied for the proposed bio-inspired quadrilateral shape structure system (BIQS) under either periodic or impulsive external excitations. Compared with the traditional SMD isolator, the proposed BIQS system can be regarded as a highly efficient passive control method for vibration suppression of free-floating spacecraft.

Nonetheless, there still exists many problems in the aspects of reliability and stability for pure passive X-shape structure vibration control. For example, the pure passive structure is easily vulnerable to some uncertainties and the drifting problem illustrated in Dai et al. [Dai, Jing, Wang et al. (2018)] makes spacecraft be in a state of instability. Therefore, that how to achieve higher reliability and stability is crucial in complex space environment. It is very necessary to add the active control into the X-shape structure system to achieve better vibration isolation performance.

In this work, the bio-inspired X-shape structure between the robotic arm and the capturing mechanism is redesigned in order to improve the stability of system by adding the sliding tracks into both sides, which can change one-point into two-point supporting. Besides, a hybrid passive/active vibration isolation control strategy is proposed to suppress the post-capture vibrations of the loosely connected combined spacecraft system consisting of a chaser, a target and an X-shape isolator. The adaptive control method through dynamic

scaling technique introduced in Seo et al. [Seo and Akella (2008); Bustan, Sani and Pariz (2014); Karagiannis, Sassano and Astolfi (2009); Liu, Ortega, Su et al. (2011); Wen, Yue and Yuan (2017); Wen, Yue, Li et al. (2017)] is adopted as the active control component in the present hybrid control method. When the end-effector of spacecraft is subjected to the external impulsive force, the X-shape structure vibration isolation system without active control can suppress vibrations efficiently, but the whole combined system may drift at a certain speed. With the introduction of active control strategy, the drifting problem arose in the X-shape structure system can be conquered. Overall, the main contributions of this study are two-folds: (i) the hybrid passive/active vibration control strategy based on the bio-inspired X-shape structure is first proposed to suppress the post-capture vibrations of the free-floating spacecraft subjected to the impact excitation; (ii) the adaptive controller through dynamic scaling technique is designed for the X-shape isolation system with parameter uncertainties, which shows a much better performance.

The rest of this paper is organized as follows. In Section 2, the dynamical equations for the X-shape structure isolation system are formulated. The main design procedures of the adaptive control are presented in Section 3. In Section 4, numerical simulations based on the dynamical model in Section 2 are presented to show the validity and feasibility of this hybrid control strategy. Finally, a conclusion is drawn to summarize the results.

2 Problem statement

When the spacecraft is performing the on-orbit capturing missions, the capture mechanism has a collision with the target inevitably, which generates the impact excitation on the end-effector. This is especially the case for some uncooperative targets, which lack accurate state information and result in some undesirable vibrations that can do damage to the satellite platform. Therefore, we combine the X-shape structure in conjunction with active control method to suppress generated vibrations to make the satellite platform become stable as quickly as possible.

In this Section, we consider the passive vibration isolation system with an n-layer X-shape

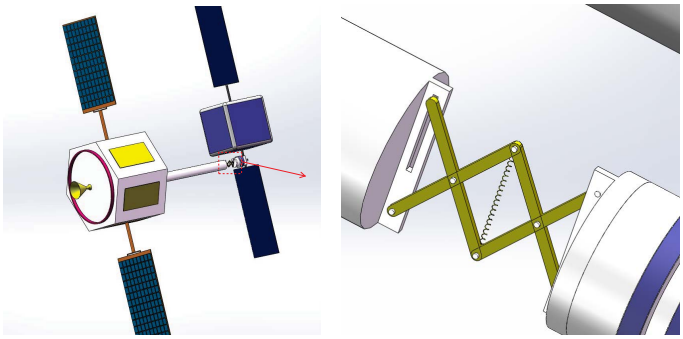

(a) Global view (b) Local view

Figure 1: Schematic diagram of implementing capture mission of spacecraft with the X-shape structure

structure. The X-shape structure is installed between the robotic arm and the capture mechanism. The schematic diagram of the n-layer X-shape structure isolation system is depicted in Fig. 1. Different from the designed X-shape structure in Dai et al. [Dai, Jing, Wang et al. (2018)], the X-shape structure in this paper is modified by adding two sliding tracks in both sides, which changes the one-point into two-point support, which improves the stability of the whole system. Here the mass m represents the capture mechanism including the end-effector and the target, and the mass M denotes the satellite platform with the robotic arm. Besides, each layer has two rods in combination with one joint whose length of each rod is $2l$. The angle between the rod and the vertical line is denoted as θ. The angle displacement of each connecting joint is represented by φ and z is the vertical motion of each connecting joint. The two supporting joints in the left and right bottom layer can freely slide along with pre-designed vertical tracks. The restoring force in the vertical spring is linear with the stiffness k_l. The undeformed and deformed states of the whole isolation system are shown in Fig. 2. The absolute displacement of the satellite platform and the capture mechanism are denoted by x and y, respectively. All variables of the X-shape isolation system are marked in Fig. 2. It can be seen that the n-layer X-shape structure is a two-degree-of-freedom system because the rotational angle φ and vertical motion z can be expressed by x and y. According to the geometrical relations of the connecting rods and the relative motions, the rotating angle φ and the vertical motion z are determined by

$$\varphi = \theta - \arctan\left(\frac{l\sin\theta - \frac{y-x}{2n}}{l\cos\theta + z/2}\right) \tag{1}$$

$$z = 2\sqrt{l^2 - \left(l\sin\theta - \frac{y-x}{2n}\right)^2} - 2l\cos\theta \tag{2}$$

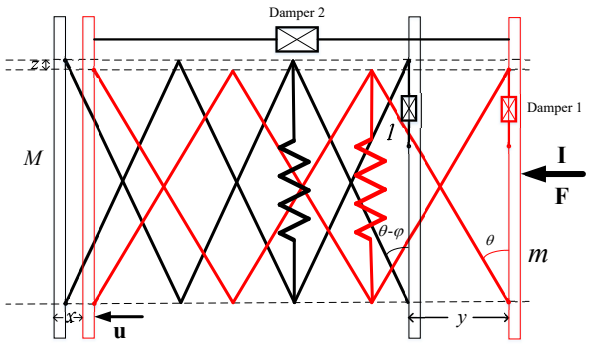

Figure 2: The undeformed (red) and deformed (black) states of the X-shape structure

It should be noted that the masses of the connecting rods and the joints in the X-shape structure system are neglected because they are far lighter than the capture mechanism and the satellite platform. The absolute motions x and y of the masses M and m are chosen as

the generalized coordinates. The kinetic energy of the whole system can be written as:

$$T = \frac{1}{2}M\dot{x}^2 + \frac{1}{2}m\dot{y}^2 \tag{3}$$

The potential energy is the elastic energy of the spring in the X-shape structure in the vertical direction, which can be expressed as:

$$V = \frac{1}{2}k_l z^2 \tag{4}$$

where k_l denotes the stiffness of spring and z is the motion along the pre-designed sliding track.

The virtual work δW is given by:

$$\delta W = -c_1(\dot{y} - \dot{x})\delta(y - x) - 6nc_2\dot{\varphi}\delta\varphi + u\delta x + F\delta y \tag{5}$$

where c_1 is the damping coefficient in the horizontal direction and c_2 is the rotational friction coefficient of each connecting joint. The impulsive force on y is represented by F and the active control torque over x is denoted by u, which can be generated either by gas jets or by reaction wheels mounted on the spacecraft. The generalized forces Q_x and Q_y are defined as follows:

$$Q_x = c_1(\dot{y} - \dot{x}) - 6nc_2\dot{\varphi}\frac{\partial\varphi}{\partial x} + u \tag{6}$$

$$Q_y = -c_1(\dot{y} - \dot{x}) - 6nc_2\dot{\varphi}\frac{\partial\varphi}{\partial y} + F \tag{7}$$

Making use of the Lagrange's principle, the governing equations of the hybrid vibration isolation system which is subjected to the control force and the external excitation can be determined as follows:

$$M\ddot{x} + k_l z\frac{\partial z}{\partial x} + c_1(\dot{x} - \dot{y}) + 6nc_2\dot{\varphi}\frac{\partial\varphi}{\partial x} = u \tag{8}$$

$$m\ddot{y} + k_l z\frac{\partial z}{\partial y} + c_1(\dot{y} - \dot{x}) + 6nc_2\dot{\varphi}\frac{\partial\varphi}{\partial y} = F \tag{9}$$

According to the Eqs. (1) and (2), the above dynamical equations can be transformed in terms of x and y as:

$$M\ddot{x} + \left(c_1 + \frac{3c_2}{2n[l^2 - (l\sin\theta - \frac{y-x}{2n})^2]}\right)(\dot{x} - \dot{y}) + \frac{k_l}{n^2}(y - x) + \frac{2k_l l\cos\theta}{n}\frac{l\sin\theta - \frac{y-x}{2n}}{\sqrt{l^2 - (l\sin\theta - \frac{y-x}{2n})^2}} - \frac{2k_l l\sin\theta}{n} = u \tag{10}$$

$$m\ddot{y} + \left(c_1 + \frac{3c_2}{2n[l^2 - (l\sin\theta - \frac{y-x}{2n})^2]}\right)(\dot{y} - \dot{x}) - \frac{k_l}{n^2}(y - x) - \frac{2k_l l\cos\theta}{n}\frac{l\sin\theta - \frac{y-x}{2n}}{\sqrt{l^2 - (l\sin\theta - \frac{y-x}{2n})^2}} + \frac{2k_l l\sin\theta}{n} = F \tag{11}$$

Employing the third order Taylor expansion series, the dynamical equations can be changed into:

$$\begin{aligned} M\ddot{x} - [\alpha_0 + \alpha_1(y-x) + \alpha_2(y-x)^2 + \alpha_3(y-x)^3](\dot{y}-\dot{x}) \\ -[\beta_1(y-x) + \beta_2(y-x)^2 + \beta_3(y-x)^3 + \beta_4(y-x)^4] = u \\ m\ddot{y} + [\alpha_0 + \alpha_1(y-x) + \alpha_2(y-x)^2 + \alpha_3(y-x)^3](\dot{y}-\dot{x}) \\ +[\beta_1(y-x) + \beta_2(y-x)^2 + \beta_3(y-x)^3 + \beta_4(y-x)^4] = F \end{aligned} \tag{12}$$

where

$$\alpha_0 = c_1 + \frac{3c_2}{2nl^2}\sec^2\theta, \tag{13}$$

$$\alpha_1 = -\frac{3c_2}{2n^2l^3}\tan\theta\sec^3\theta, \tag{14}$$

$$\alpha_2 = \frac{3c_2}{8n^3l^4}\sec^4\theta(4\sec^2\theta - 3), \tag{15}$$

$$\alpha_3 = -\frac{3c_2}{4n^4l^5}\tan\theta\sec^5\theta(2\sec^2\theta + 1) \tag{16}$$

and

$$\beta_1 = \frac{k_l}{n^2}(\sec^2\theta - 1), \tag{17}$$

$$\beta_2 = -\frac{3k_l}{4n^3l}\tan\theta\sec^3\theta, \tag{18}$$

$$\beta_3 = \frac{k_l}{8n^4l^2}\sec^6\theta(4\sin^2\theta + 1), \tag{19}$$

$$\beta_4 = -\frac{5k_l}{64n^5l^3}\sin\theta\sec^8\theta(4\sin^2\theta + 3) \tag{20}$$

In this study, parameters of the hybrid vibration isolation systems except c_1, c_2 and M are all known. The aim is to control the velocity and displacement of the satellite platform M to keep it stable when the end-effector is subjected to the impulsive excitation. To achieve this goal, considering the parameter uncertainties of system, an adaptive controller through dynamic scaling design is selected as an active control component, which is explained in detail in the next Section.

3 Adaptive control through dynamic scaling design

To illustrate this control strategy more clearly, the above case is extended to a general one. The dynamical model of an n-degree-of-freedom Euler-Lagrange system can be expressed as follows:

$$\dot{x}_1 = x_2 \tag{21}$$

$$M(x_1,\theta)\dot{x}_2 + C(x_1,x_2,\theta)x_2 + G(x_1,\theta) = u \tag{22}$$

where $x_1 = [x_{11}, \quad x_{12}, \quad \ldots, \quad x_{1n}]^T \in \mathbb{R}^n$ and $x_2 = [x_{21}, \quad x_{22}, \quad \ldots, \quad x_{2n}]^T \in \mathbb{R}^n$ are the generalized position and velocity vectors, respectively. $\theta = [p_1, \quad p_2, \quad \ldots, \quad p_m]^T \in \mathbb{R}^m$ represents the unknown system parameters, which means that both $M(x_1,\theta)$ and

$C(x_1, x_2, \theta)$ are unknown. $u \in \mathbb{R}^n$ is the vector of the control torques. The following properties [Seo and Akella (2009)] of the system defined in Eqs. (21) and (22) are satisfied:

(1) Both $M(x_1, \theta)$ and $C(x_1, x_2, \theta)$ are linear in terms of θ, which can be stated as:

$$M(x_1, \theta)\, x + C(x_1, x_2, \theta)\, y + G(x_1, \theta) = W(x_1, x_2)\, \theta, \quad \forall x, y \in \mathbb{R}^n \tag{23}$$

(2) $M(x_1, \theta)$ is a real positive-definite symmetric matrix such that

$$\lambda_{\min} \|x\|^2 \leq x^T M(x_1, \theta)\, x \leq \|M(x_1, \theta)\| \|x\|^2, \quad \forall x \in \mathbb{R}^n \tag{24}$$

where $\lambda_{\min} > 0$ is a constant which denotes the minimum eigenvalue of $M(x_1, \theta)$. $\| \bullet \|$ represents the 2-norm here and hereafter. Considering a smooth and bounded reference trajectory $x_d \in \mathbb{R}^n$ whose first to third-order derivatives are also smooth and bounded, the tracking errors $x_e = [x_{1e}, x_{2e}]^T \in \mathbb{R}^{2n}$ can be defined as $x_{1e} = x_1 - x_d$ and $x_{2e} = x_2 - \dot{x}_d$, respectively. As a consequence, the overall tracking error dynamics are obtained as:

$$\dot{x}_{1e} = x_{2e} \tag{25}$$

$$M(x_1, \theta)\, \dot{x}_{2e} = -M(x_1, \theta)\, \ddot{x}_d - C(x_1, x_2, \theta)\, x_2 - G(x_1, \theta) + u \tag{26}$$

Assuming that the relative displacement and the relative velocity measurements are all available, the aim in this study is to design a tracking controller that will ensure the asymptotic convergence of the tracking errors, which can be stated as $\lim_{t \to \infty} x_e = 0$.

Next, an adaptive control method through the dynamic scaling technique is designed. The main procedures are presented in the following parts.

3.1 The generalized velocity observer

For the system given in Eqs. (25) and (26), the parameter estimation error is defined as:

$$z_f = \varepsilon + \beta - \theta \tag{27}$$

where $\varepsilon, \beta \in \mathbb{R}^m$ are the functions to be specified. A generalized velocity observer is constructed to modify the traditional Immersion & Invariance parameter estimation procedure, which is designed as:

$$\dot{\hat{x}}_2 = \ddot{x}_d - \alpha x_{1e} - (k_e + \delta_x)\, x_{2e} - \psi_{\hat{x}} (\hat{x}_2 - x_2) \tag{28}$$

where $\hat{x}_2 = [\hat{x}_{21}, \quad \hat{x}_{22}, \quad \ldots, \quad \hat{x}_{2n}] \in \mathbb{R}^n$ denotes the estimated values of x_2. $k_e \in \mathbb{R}$ and $\psi_{\hat{x}} \in \mathbb{R}$ are the gains to be determined. Both δ_x and α are positive constants. Regarding a regression matrix $W(x_2, x_1, x_d, \dot{x}_d, \ddot{x}_d, k_e) \in \mathbb{R}^{n \times m}$ as an "ideal" solution of $\left(\dfrac{\partial \beta}{\partial x_2} \right)^T$, we can obtain:

$$W\theta = -M\ddot{x}_d - Cx_2 - G + \alpha M x_{1e} + (k_e + \delta_x)\, M x_{2e} \tag{29}$$

By utilizing $\hat{x}_2$ and the elements of W, we can generate an "approximate" solution $\beta = \beta(x_2, \hat{x}_2, x_1, x_d, \dot{x}_d, \ddot{x}_d, k_e)$ as follow:

$$\beta = \gamma \sum_{i=1}^{n} W_i (\hat{x}_2, x_1, x_d, \dot{x}_d, \ddot{x}_d, k_e)\, x_{2i} \tag{30}$$

where $\gamma > 0$ is a constant. $W^T = \Big[W_1, W_2, \ldots, W_n\Big]$, where $W_1, W_2, \ldots, W_n \in \mathbb{R}^{m\times 1}$ are the column vectors of $W^T \in \mathbb{R}^{m\times n}$. On the assumption that k_e is independent of x_2, the dynamics of z_f can be obtained by substituting Eqs. (21), (22) and (30) into the time derivative of Eq. (27):

$$\begin{aligned}\dot{z}_f = \dot{\varepsilon} + \frac{\partial\beta}{\partial\hat{x}_2}\dot{\hat{x}}_2 + \frac{\partial\beta}{\partial x_1}x_2 + \frac{\partial\beta}{\partial x_d}\dot{x}_d + \frac{\partial\beta}{\partial\dot{x}_d}\ddot{x}_d + \frac{\partial\beta}{\partial\ddot{x}_d}x_d^{(3)} + \frac{\partial\beta}{\partial k_e}\dot{k}_e \\ + \frac{\partial\beta}{\partial x_2}M^{-1}\left(-Cx_2 - G + u\right)\end{aligned} \tag{31}$$

From Eq. (30), $\dfrac{\partial\beta}{\partial x_2}$ is obtained as

$$\frac{\partial\beta}{\partial x_2} = \gamma W^T + \gamma\Big[W\left(\hat{x}_2, x_1, x_d, \dot{x}_d, \ddot{x}_d, k_e\right) - W\Big]^T \tag{32}$$

Considering that all functions in Eq. (32) are smooth and $\dfrac{\partial\beta}{\partial x_2} = \gamma W^T$ holds when $\hat{x}_2 = x_2$, there exists a smooth mapping $\Delta_x\left(\hat{x}_2 - x_2, x_1, x_2, \hat{x}_2, x_d, \dot{x}_d, \ddot{x}_d, k_e\right)$ that satisfies:

$$\frac{\partial\beta}{\partial x_2} = \gamma\Big[W + \Delta_x\left(\hat{x}_2 - x_2, x_1, x_2, \hat{x}_2, x_d, \dot{x}_d, \ddot{x}_d, k_e\right)\Big]^T \tag{33}$$

such that

$$\Delta_x\left(0, x_1, x_2, \hat{x}_2, x_d, \dot{x}_d, \ddot{x}_d, k_e\right) = 0 \tag{34}$$

holds for all $x_1, x_2, \hat{x}_2, x_d, \dot{x}_d, \ddot{x}_d \in \mathbb{R}^n$ and $k_e \in \mathbb{R}$. Furthermore, Eq. (34) ensures the existence of the mapping $\bar{\Delta}_x\left(x_1, x_2, \hat{x}_2, x_d, \dot{x}_d, \ddot{x}_d, k_e\right)$ such that

$$\|\Delta_x\|^2 \le \|\bar{\Delta}_x\left(x_1, x_2, \hat{x}_2, x_d, \dot{x}_d, \ddot{x}_d, k_e\right)\|\|\hat{x}_2 - x_2\|^2 \tag{35}$$

The detailed proof for the existence of Δ_x and $\bar{\Delta}_x$ is included in the simulation section with respect to the above system. In view of Eqs. (29), (31) and (33), $\dot{z}_f$ is turned into

$$\begin{aligned}\dot{z}_f = \dot{\varepsilon} + \frac{\partial\beta}{\partial\hat{x}_2}\dot{\hat{x}}_2 + \frac{\partial\beta}{\partial x_1}x_2 + \frac{\partial\beta}{\partial x_d}\dot{x}_d + \frac{\partial\beta}{\partial\dot{x}_d}\ddot{x}_d + \frac{\partial\beta}{\partial\ddot{x}_d}x_d^{(3)} + \frac{\partial\beta}{\partial k_e}\dot{k}_e \\ + \gamma\left(W + \Delta_x\right)^T\Big[\ddot{x}_d - \alpha x_{1e} - \left(k_e + \delta_x\right)x_{2e}\Big] + \gamma\left(W + \Delta_x\right)^T M^{-1}\left(W\theta + u\right)\end{aligned} \tag{36}$$

Let the estimation law $\dot{\varepsilon}$ and the control law u be assigned as:

$$\begin{aligned}\dot{\varepsilon} = -\frac{\partial\beta}{\partial\hat{x}_2}\dot{\hat{x}}_2 - \frac{\partial\beta}{\partial x_1}x_2 - \frac{\partial\beta}{\partial x_d}\dot{x}_d - \frac{\partial\beta}{\partial\dot{x}_d}\ddot{x}_d - \frac{\partial\beta}{\partial\ddot{x}_d}x_d^{(3)} - \frac{\partial\beta}{\partial k_e}\dot{k}_e \\ - \gamma\left(W + \Delta_x\right)^T\Big[\ddot{x}_d - \alpha x_{1e} - \left(k_e + \delta_x\right)x_{2e}\Big]\end{aligned} \tag{37}$$

$$u = -W\left(\varepsilon + \beta\right) \tag{38}$$

Then the Eq. (36) is reduced to

$$\begin{aligned}\dot{z}_f &= -\gamma W^T M^{-1} W z_f - \gamma\Delta_x^T M^{-1} W z_f \\ &= -\gamma W^T M^{-1} W z_f - \phi\left(\Delta_x\right)\end{aligned} \tag{39}$$

From the structure of Eq. (39), it can be concluded that $\phi\left(\Delta_x\right)$ acts as a "disturbance" to the convergence of z_f, so we will focus on the elimination of this "disturbance" in the next part.

3.2 Dynamic scaling

Assuming that there exists a scalar function $r(t)$ satisfying $r(t) \geq 1$ for $\forall t \geq 0$, a scaled parameter estimation error is considered as follows:

$$z = \frac{z_f}{e^{\frac{\sqrt{\ln r+1}}{\lambda_{\min}}}} \cdot \frac{e^{\frac{1}{2}\left(\frac{1}{\lambda_{\min}^2}+1\right)}}{\sqrt{\lambda_{\min}}} \tag{40}$$

where $\lambda_{\min}$ is defined in Eq. (24).
The derivative of z with respect to time is obtained as:

$$\dot{z} = \frac{\dot{z}_f}{e^{\frac{\sqrt{\ln r+1}}{\lambda_{\min}}}} \cdot \frac{e^{\frac{1}{2}\left(\frac{1}{\lambda_{\min}^2}+1\right)}}{\sqrt{\lambda_{\min}}} - \frac{\dot{r}}{2\lambda_{\min} r\sqrt{\ln r+1}} \cdot z \tag{41}$$

Substituting Eqs. (39) and (40) into (41) yields

$$\dot{z} = -\gamma W^T M^{-1} W z - \gamma \Delta_x^T M^{-1} W z - \frac{\dot{r}}{2\lambda_{\min} r\sqrt{\ln r+1}} \cdot z \tag{42}$$

Consider a positive semi-definite Lyapunov function as:

$$V_z = \frac{1}{2\gamma} z^T z \tag{43}$$

then $\dot{V}_z$ can be obtained:

$$\begin{aligned} \dot{V}_z &= -z^T W^T M^{-1} W z - z^T \Delta_x^T M^{-1} W z - \frac{\dot{r}}{2\gamma\lambda_{\min} r\sqrt{\ln r+1}} z^T z \\ &\leq -\frac{\lambda_{\min}}{2}\|M^{-1} W z\|^2 + \frac{\|z\|^2}{\lambda_{\min}}\left(\frac{\|\Delta_x\|^2}{2} - \frac{\dot{r}}{2\gamma r\sqrt{\ln r+1}}\right) \end{aligned} \tag{44}$$

Let

$$\dot{r} = \gamma r\sqrt{\ln r+1}\|\Delta_x\|^2 \tag{45}$$

From Eq. (45), it can be concluded that r is a monotone increasing function. So $r(0) \geq 1$ must be satisfied to ensure $r(t) \geq r(0) \geq 1$. Substituting Eq. (45) into Eq. (44) yields

$$\dot{V}_z \leq -\frac{\lambda_{\min}}{2}\|M^{-1} W z\|^2 \tag{46}$$

From Eq. (46), we have $M^{-1} W z \in \mathcal{L}_2$ and $z \in \mathcal{L}_\infty$. It is worth noting that $z \in \mathcal{L}_\infty$ does not imply $z_f \in \mathcal{L}_\infty$ because of $z_f = e^{\frac{\sqrt{\ln r+1}}{\lambda_{\min}}} \cdot \frac{\sqrt{\lambda_{\min}}}{e^{\frac{1}{2}\left(\frac{1}{\lambda_{\min}^2}+1\right)}} \cdot z$. Therefore, we will concentrate on the boundedness of r, $\hat{x}_2 - x_2$, x_{1e} and x_{2e} in the following step.

3.3 Domination of the closed-loop errors

From Eqs. (25), (26), (28) and (45), we consider the following Lyapunov functions

$$V_e = \frac{1}{2}x_{2e}^T x_{2e} + \frac{\alpha}{2}x_{1e}^T x_{1e} \tag{47}$$

$$V_{\hat{x}} = \frac{1}{2}\left(\hat{x}_2 - x_2\right)^T\left(\hat{x}_2 - x_2\right) \tag{48}$$

$$V_r = \frac{k_{\hat{x}}}{\gamma}\sqrt{\ln r + 1} \tag{49}$$

where $k_{\hat{x}} > 0$ is a constant. Note that we have selected $r\left(0\right) \geq 1$, which ensures that V_r is positive definite. In combination with Eqs. (22), (25), (26), (38), (40) and (48), $\dot{V}_{\hat{x}}$ can be expressed as:

$$\dot{V}_{\hat{x}} = \left(\hat{x}_2 - x_2\right)^T M^{-1}W z_f - \psi_{\hat{x}}\left(\hat{x}_2 - x_2\right)^T\left(\hat{x}_2 - x_2\right) \tag{50}$$

Due to $r(0) \geq 1$, the following inequality exists according to Eq. (45):

$$e^{\frac{\sqrt{\ln r+1}}{\lambda_{\min}}} \leq e^{\frac{1}{2\lambda_{\min}^2}+\frac{\ln r+1}{2}} \leq e^{\frac{1}{2}\left(\frac{1}{\lambda_{\min}^2}+1\right)}\sqrt{r} \tag{51}$$

Substituting Eq. (40) into Eq. (50) and making use of Eq. (51) yields

$$\begin{aligned}
\dot{V}_{\hat{x}} &= e^{\frac{\sqrt{\ln r+1}}{\lambda_{\min}}} \cdot \frac{\sqrt{\lambda_{\min}}}{e^{\frac{1}{2}\left(\frac{1}{\lambda_{\min}^2}+1\right)}}\left(\hat{x}_2 - x_2\right)^T M^{-1}W z - \psi_{\hat{x}}\|\hat{x}_2 - x_2\|^2 \\
&\leq \frac{1}{2}\left[\frac{e^{\frac{\sqrt{\ln r+1}}{\lambda_{\min}}}}{e^{\frac{1}{2}\left(\frac{1}{\lambda_{\min}^2}+1\right)}}\right]^2\|\hat{x}_2 - x_2\|^2 + \frac{\lambda_{\min}}{2}\|M^{-1}Wz\|^2 - \psi_{\hat{x}}\|\hat{x}_2 - x_2\|^2 \\
&\leq \left(\frac{1}{2}r - \psi_{\hat{x}}\right)\|\hat{x}_2 - x_2\|^2 + \frac{\lambda_{\min}}{2}\|M^{-1}Wz\|^2
\end{aligned} \tag{52}$$

Let $V_1 = V_z + V_{\hat{x}} + V_r$, then employing Eqs. (35), (46) and (52), $\dot{V}_1$ is obtained as follows:

$$\dot{V}_1 = \dot{V}_z + \dot{V}_{\hat{x}} + \dot{V}_r \leq \left(\frac{1}{2}r - \psi_{\hat{x}} + \frac{k_{\hat{x}}}{2}\|\bar{\Delta}_x\|\right)\|\hat{x}_2 - x_2\|^2 \tag{53}$$

Select the gain $\psi_{\hat{x}}$ as

$$\psi_{\hat{x}} = \frac{1}{2}r + \frac{k_{\hat{x}}}{2}\|\bar{\Delta}_x\| \tag{54}$$

then we have

$$\dot{V}_1 \leq 0 \tag{55}$$

From Eq. (55), we can obtain $\hat{x}_2 - x_2, r \in \mathcal{L}_\infty$, which indicates that $z_f \in \mathcal{L}_\infty$ and $M^{-1}Wz_f \in \mathcal{L}_2$ because of the facts $z_f = e^{\frac{\sqrt{\ln r+1}}{\lambda_{\min}}} \cdot \frac{\sqrt{\lambda_{\min}}}{e^{\frac{1}{2}\left(\frac{1}{\lambda_{\min}^2}+1\right)}}z$, $z \in \mathcal{L}_\infty$ and $M^{-1}Wz \in \mathcal{L}_2$. Furthermore, from Eqs. (22) and (28), $\lim_{t\to\infty}\hat{x}_2 - x_2 = 0$ can be acquired by utilizing Barbalat's lemma. In a word, the proposed controller ensures the asymptotic convergence

of the observation error and the boundedness of r, and the asymptotic convergence of the tracking error x_{1e} and x_{2e} can also be proved in a similar way. According to Eq. (47), $\dot{V}_e$ can be obtained as:

$$\begin{aligned}\dot{V}_e &= x_{2e}^T M^{-1}\left[-Wz_f-\left(k_e+\delta_x\right)Mx_{2e}-\alpha Mx_{1e}\right]+\alpha x_{1e}^T x_{2e}\\ &= -x_{2e}^T M^{-1}Wz_f-k_e\|x_{2e}\|^2-\delta_x\|x_{2e}\|^2\end{aligned} \tag{56}$$

Substituting Eq. (40) into Eq. (56) yields

$$\begin{aligned}\dot{V}_e &= -e^{\frac{\sqrt{\ln r+1}}{\lambda_{\min}}}\cdot\frac{\sqrt{\lambda_{\min}}}{e^{\frac{1}{2}\left(\frac{1}{\lambda_{\min}^2}+1\right)}}x_{2e}^T M^{-1}Wz-k_e\|x_{2e}\|^2\\ &\le\left(\frac{1}{2}r-k_e\right)\|x_{2e}\|^2+\frac{\lambda_{\min}}{2}\|M^{-1}Wz\|^2-\delta_x\|x_{2e}\|^2\end{aligned} \tag{57}$$

Select the gain k_e as:

$$k_e=\frac{1}{2}r \tag{58}$$

Let $V_2=V_z+V_e$, then employing Eqs. (46), (57) and (58), the derivative of V_2 with respect to time is given as:

$$\dot{V}_2=\dot{V}_z+\dot{V}_e\le-\delta_x\|x_{2e}\|^2 \tag{59}$$

which demonstrates that $x_{1e}\in\mathcal{L}_\infty$ and $x_{2e}\in\mathcal{L}_2\bigcap\mathcal{L}_\infty$. From Eqs. (25), (26), (29) and (38), $\dot{x}_{2e}$ can be further written as:

$$\dot{x}_{2e}=-M^{-1}Wz_f-\left(k_e+\delta_x\right)x_{2e}-\alpha x_{1e} \tag{60}$$

Considering that $M^{-1}Wz_f\in\mathcal{L}_2$, we can obtain that $\lim\limits_{t\to\infty}x_{2e}=0$ by utilizing Barbalat's lemma. From Eqs. (26), (29) and (39), we can prove that $\ddot{x}_{2e}$ is bounded because $\dot{z}_f$, $\dot{W}$ and $M\left(x_1,\theta\right)$ are bounded, which also implies that $\lim\limits_{t\to\infty}\dot{x}_{2e}=0$ and $\lim\limits_{t\to\infty}M^{-1}Wz_f=0$. Therefore, we have $\lim\limits_{t\to\infty}x_{1e}=0$ from Eq. (60). All in all, this designed controller ensures the asymptotic convergence of the tracking errors.

4 Numerical simulation

In this Section, an adaptive method as active control component is employed in the vibration isolation system introduced in Section 2 and numerical simulations are used to demonstrate the validity and feasibility of this hybrid control strategy. Here we pay more attentions to the vibration responses of the satellite platform which consists of many precision instruments. Therefore, we only apply the adaptive controller into vibration suppression of the satellite platform.

4.1 Comparison with SMD isolator under no control

Before exerting control force into the system, we first observe that how responses of the X-shape structure system change without control. The SMD isolator is widely used for vibration isolation in practice. Therefore, we make a comparison between the uncontrolled

X-shape structure system and the uncontrolled SMD isolator in details. The dynamical model of the SMD isolator with the same technique represented in Section 2 is given as follows.

$$M\ddot{x} - c(\dot{y} - \dot{x}) - k(y - x) = 0 \tag{61}$$

$$m\ddot{y} + c(\dot{y} - \dot{x}) + k(y - x) = F \tag{62}$$

It should be noted that we must select the system parameters of the SMD isolator legitimately in order to ensure a fair comparison between the X-shape structure isolation system and the traditional SMD isolator, so the linearized damping α_0 and the linearized stiffness β_1 in Eq. (12) are regarded as the damping coefficient c and stiffness of spring k, respectively. The displacement transmissibility represented by T_d is thought as a reliable measure of vibration control system and defined as the ratio between the vibration amplitude of the mass M and that of the mass m, i.e., $T_d = A_M/A_m$. Here M=100 kg, m=2 kg, k_l=1200 N/m, $\theta = \pi/6$, l=0.2 m, n=3. In order to compare the X-shape system with the SMD isolator better, the force F is selected as the periodic external excitation, i.e., $F = A\cos(\omega t)$, where $A = 2$, $\omega \in [0, 10]$. The parameters given above are fixed as reference unless otherwise specified. The displacement transmissibility versus forcing frequency curves for X-shape structure and SMD isolators are depicted in Fig. 3. As we can see from this figure, the two curves coincide basically except in the resonant frequency region. The magnified part denotes that the maximum displacement transmissibility of the X-shape structure and the SMD isolators are 6.914 dB and 9.634 dB, respectively. Besides, the resonant frequency of the X-shape structure system is smaller than that of the SMD isolator. A conclusion can be drawn that the X-shape structure system has better vibration isolation performance than SMD isolator around the natural frequency. In the higher frequency region, there exists the lower displacement transmissibility for the X-shape structure system, which is less obvious than around natural frequency region.

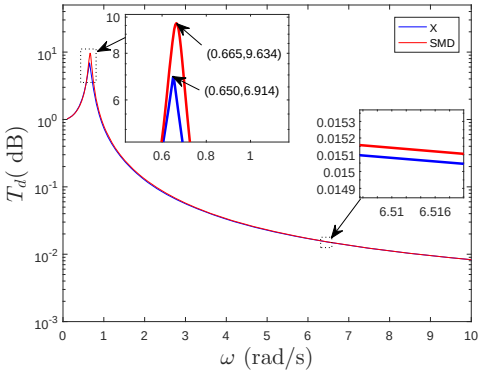

Figure 3: Displacement transmissibility versus forcing frequency between the X-shape structure and SMD isolators without control

Next, the vibration responses are investigated for two vibration isolation systems when subjected to an impulsive force. To simulate the post-capture responses better, the

impulsive force F is replaced by imposing an impulse I to the end-effector where the impulse I is selected as $I = 0.8$ kg $\cdot m/s$. It means that the capture mechanism is provided a initial velocity with influence of the impulsive force F, because the acting time of the impulsive force is infinitesimal. Figs. 4 and 6 show the absolute displacement of the satellite platform M and the capture mechanism m, respectively. It can be seen that the curves of X-shape structure system are in agreement with that of SMD isolator basically. With time going by, the displacement x as well as y is still increasing and approaches to a oblique line, which implies that the motion consists of simultaneous vibrational and translational components. Due to the existence of damping, vibration response stops after a short period of time. Shown in Figs. 5 and 7 are the velocities of them, two curves jump up and down in the first few seconds and keep constant afterwards, which indicates that the two masses do not keep stable and drift at a speed v_d = 0.78 cm/s ultimately. The accelerations of the masses m and M for the X-shape structure and SMD isolator are plotted in Figs. 8 and 9, respectively. It can be seen that the maximum accelerations of $\ddot{y}$ for the X-shape and SMD isolator are 1.50 m/s^2 and 1.57 m/s^2, and that of $\ddot{x}$ are 0.0300 m/s^2 and 0.0315 m/s^2. $|\ddot{y}|_{max}$ and $|\ddot{x}|_{max}$ of the SMD isolator are 4.7% and 5.1% larger than that of the X-shape structure system. It indicates that the X-shape structure system has a better vibration isolation performance than the SMD isolator. The two pure passive isolators have a relative good vibration isolation performance for the satellite platform, but problem of drifting motion still exists and they cannot make the satellite platform stay stable, which affects the performance of the precision instruments. Thus it is very indispensable to draw the active control strategy into the X-shape isolation system to obtain better vibration isolation performance.

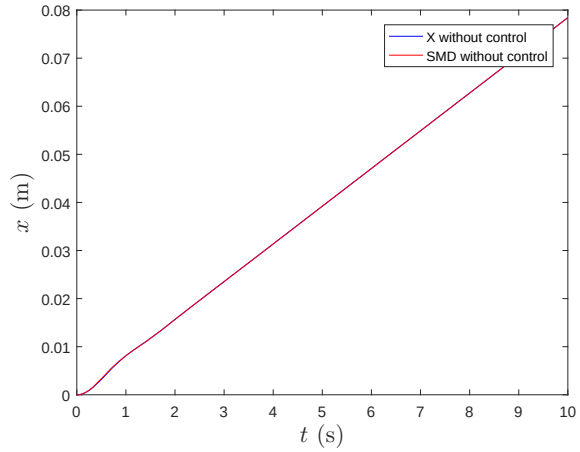

Figure 4: Absolute displacement of mass M for the X-shape structure and SMD isolators without control

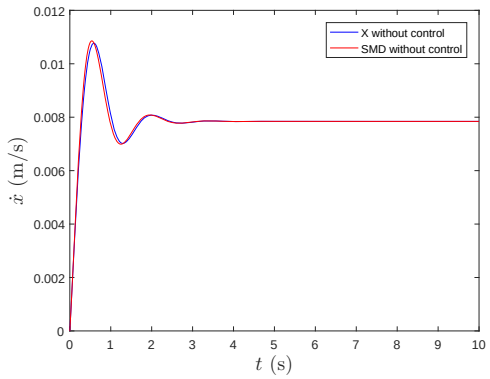

Figure 5: Velocity of mass M for the X-shape structure and SMD isolators without control

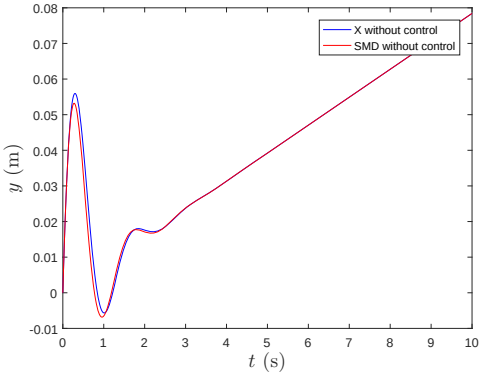

Figure 6: Absolute displacement of mass m for the X-shape structure and SMD isolators without control

4.2 Adaptive controller design

In this Section, the mass M and two structural parameters c_1, c_2 are all unknown, so that $\theta = (M, \alpha_0, \alpha_1, \alpha_2, \alpha_3)$ is also unspecified. According to the aforementioned introduction in Section 3, the parameter estimation error is defined as:

$$z_f = \varepsilon + \beta - \theta \tag{63}$$

Some related equations are given as below:

$$\dot{x_1} = x_2 \tag{64}$$

$$\dot{x_2} = M^{-1}\Big([\alpha_0 + \alpha_1(y - x_1) + \alpha_2(y - x_1)^2 + \alpha_3(y - x_1)^3](\dot{y} - x_2) + \beta_1(y - x_1) + \beta_2(y - x_1)^2 + \beta_3(y - x_1)^3 + \beta_4(y - x_1)^4 + u\Big) \tag{65}$$

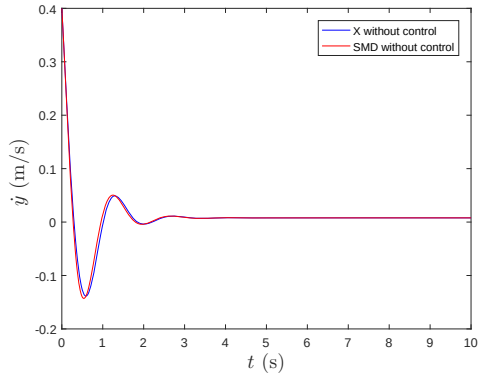

Figure 7: Velocity of mass M for the X-shape structure and SMD isolators without control

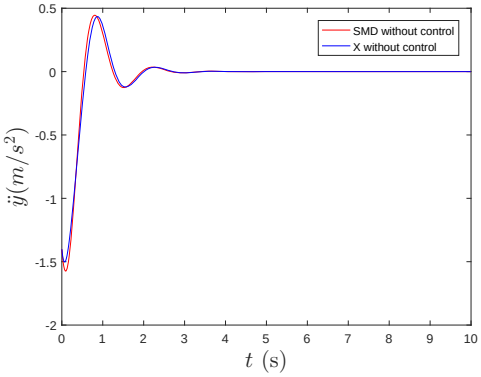

Figure 8: Acceleration of mass m for the X-shape structure and SMD isolators without control

$$M\ddot{x} - [\alpha_0 + \alpha_1(y-x) + \alpha_2(y-x)^2 + \alpha_3(y-x)^3](\dot{y}-\dot{x}) - [\beta_1(y-x) + \beta_2(y-x)^2 + \beta_3(y-x)^3 + \beta_4(y-x)^4] = u \tag{66}$$

$$W\theta = -M\ddot{x}_d + [\alpha_0 + \alpha_1(y-x) + \alpha_2(y-x)^2 + \alpha_3(y-x)^3](\dot{y}-x_2) + \alpha M x_{1e} + (k_e + \delta_x) M x_{2e} \tag{67}$$

$$\beta = \gamma W(\hat{x}_2, x_1, x_d, \dot{x}_d, \ddot{x}_d, k_e)^T x_2 \tag{68}$$

$$\frac{\partial \beta}{\partial x_2} = \gamma \left[W + \Delta_x \left(\hat{x}_2 - x_2, x_1, x_2, \hat{x}_2, x_d, \dot{x}_d, \ddot{x}_d, k_e \right) \right]^T \tag{69}$$

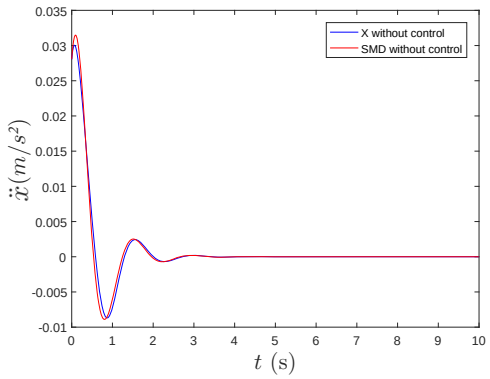

Figure 9: Acceleration of mass M for the X-shape structure and SMD isolators without control

$$\dot{z}_f = \dot{\varepsilon} + \frac{\partial\beta}{\partial\hat{x}_2}\dot{\hat{x}}_2 + \frac{\partial\beta}{\partial x_1}x_2 + \frac{\partial\beta}{\partial x_d}\dot{x}_d + \frac{\partial\beta}{\partial\dot{x}_d}\ddot{x}_d + \frac{\partial\beta}{\partial\ddot{x}_d}x_d^{(3)} + \frac{\partial\beta}{\partial k_e}\dot{k}_e + \frac{\partial\beta}{\partial x_2}M^{-1}\Big([\alpha_0 + \alpha_1(y-x) + \alpha_2(y-x)^2 + \alpha_3(y-x)^3](\dot{y}-\dot{x}) + [\beta_1(y-x) + \beta_2(y-x)^2 + \beta_3(y-x)^3 + \beta_4(y-x)^4] + u\Big) \tag{70}$$

Next, the estimation law $\dot{\varepsilon}$ and the control law u can be designed as:

$$\dot{\varepsilon} = -\frac{\partial\beta}{\partial\hat{x}_2}\dot{\hat{x}}_2 - \frac{\partial\beta}{\partial x_1}x_2 - \frac{\partial\beta}{\partial x_d}\dot{x}_d - \frac{\partial\beta}{\partial\dot{x}_d}\ddot{x}_d - \frac{\partial\beta}{\partial\ddot{x}_d}x_d^{(3)} - \frac{\partial\beta}{\partial k_e}\dot{k}_e - \gamma\left(W + \Delta_x\right)^T\left[\ddot{x}_d - \alpha x_{1e} - \left(k_e + \delta_x\right)x_{2e}\right] \tag{71}$$

$$u = -W\left(\varepsilon + \beta\right) - [\beta_1(y-x) + \beta_2(y-x)^2 + \beta_3(y-x)^3 + \beta_4(y-x)^4] \tag{72}$$

From Eqs. (67)-(69), Δ_x can be obtained as:

$$\Delta_x = \begin{bmatrix} \left(k_e + \delta_x\right)\left(\hat{x}_2 - x_2\right) \\ -\left(\hat{x}_2 - x_2\right) \\ -(y - x_1)\left(\hat{x}_2 - x_2\right) \\ -(y - x_1)^2\left(\hat{x}_2 - x_2\right) \\ -(y - x_1)^3\left(\hat{x}_2 - x_2\right) \end{bmatrix}^T \tag{73}$$

From Eq. (73), it can be obtained that

$$\Delta_x\Delta_x^T = (\hat{x}_2 - x_2)^T\bar{\Delta}_x(\hat{x}_2 - x_2) \tag{74}$$

Select the $\bar{\Delta}_x$ as:

$$\bar{\Delta}_x = (k_e + \delta_x)^2 + 1 + (y - x_1)^2 + (y - x_1)^4 + (y - x_1)^6 \tag{75}$$

Utilizing the definition of 2-norm, the following inequality from Eq. (74) can be further obtained as:

$$\|\Delta_x\Delta_x^T\| \leq \|\Delta_x\|^2 \leq \|\bar{\Delta}_x\|\|\hat{x}_2 - x_2\|^2$$

which proves the existence of Δ_x and $\overset{\Delta}{}_x$. The initial x_1, x_2, and $\hat{x}_2$ are set to zero. The reference trajectory is chosen as $x_r = 0$. The adaptive control method is included in Eqs. (28), (29), (30), (37), (38), (45), (54), (58), (73) and (75). In this numerical experiment, we employ the impulse I = 0.8 kg $\cdot m/s$ instead of the impulsive force F to simulate the post-capture dynamical response.

4.2.1 Effects of active control on the vibration isolation performance of the X-shape structure system

In this part, effects of active control strategy in combination with the X-shape structure system on the vibration isolation performance are studied in details. The dynamical equation is shown in Eq. (10). The corresponding unknown parameters are given by $\theta_X = \begin{bmatrix} 100, & 0.3, & 0.4 \end{bmatrix}^T$. The initial parameter estimate is chosen as:

$$\hat{\theta}_X(0) + \beta_X(0) = \begin{bmatrix} 120, & 0.1, & 0.3 \end{bmatrix}^T$$

The control gains are selected as follows:

$\gamma = 10$; $\alpha = 3.5$; $k_e = 2.0$; $\delta_x = 2.0$; $r\,(0) = 1.01$; $k_{\hat{x}} = 2.0$.

Next, the adaptive control is applied to the X-shape structure system. Shown in the following figures, the red line and the blue line represent the responses before and after the active control algorithm is applied, respectively. From Figs. 10 and 11, we can find that mass m can not stay stable and drift at a speed of v_d =0.78 cm/s before control, which increases the displacement of mass m. However, the drifting motion disappears and mass m tends to be stable after control. According to Figs. 12 and 13, we can see that the mass M can not keep stable after a short period of time and also drift at a speed of v_d =0.78 cm/s, which leads to increase of the displacement for mass M without control. But mass M vibrates at a very small speed initially and becomes stable in a short time under control, which protects the precision sensitive payloads from damage. The vibration isolation performance employing the active control shows advantage over the pure passive control. Therefore, it is very needful to add the adaptive control into the X-shape structure system, which can make the displacement and the velocity of the satellite platform get close to zero quickly in order to guarantee the stability.

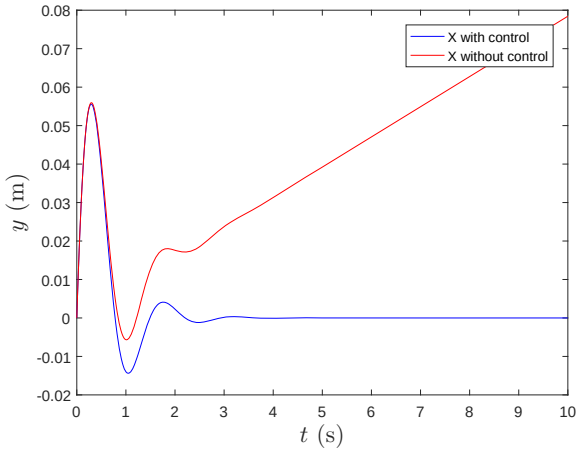

Figure 10: Displacement of mass M for the X-shape structure system with control and without control

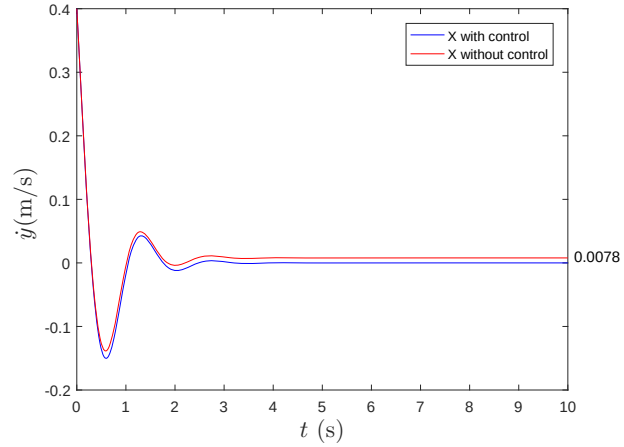

Figure 11: Velocity of mass M for the X-shape structure system with control and without control

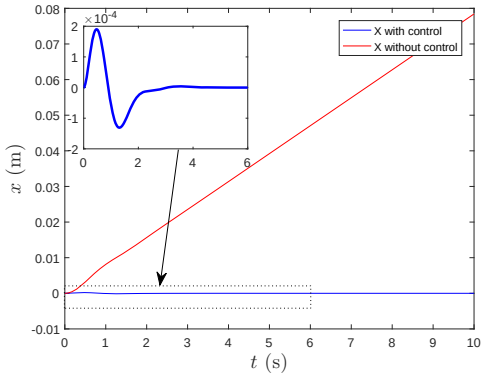

Figure 12: Displacement of mass m for the X-shape structure system with control and without control

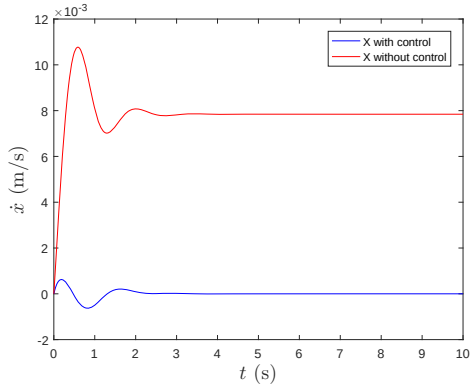

Figure 13: Velocity of mass m for the X-shape structure system with control and without control

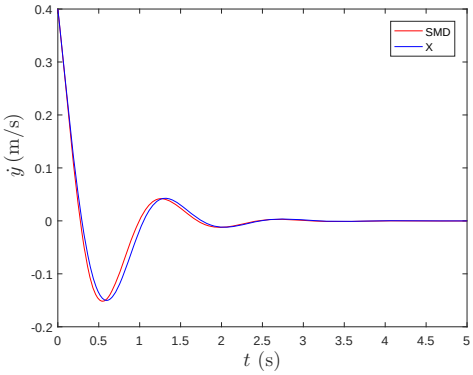

Figure 14: Velocity error of mass m for the X-shape structure and SMD isolators with control

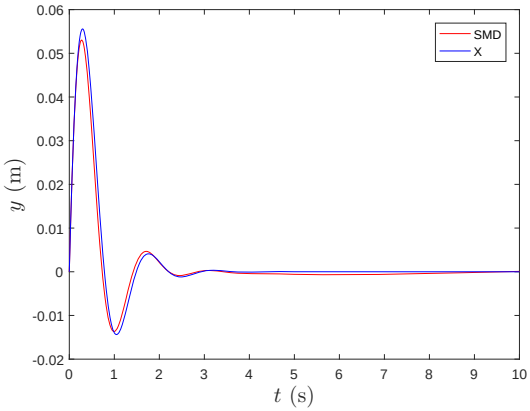

Figure 15: Displacement error of mass m for the X-shape structure and SMD isolators with control

4.2.2 Comparison with SMD isolator under control

Next, we compare the vibration isolation performance for the X-shape structure system and SMD isolator with same control scheme. The SMD dynamical equations are shown in Eqs. (61) and (62), where the corresponding unknown parameters are given by $\theta_S = \begin{bmatrix}100, & 0.3\end{bmatrix}^T$ similarly. In order to achieve a relative fair environment, the damping parameter c and the stiffness parameter k are chosen as the linearized damping α_0 in Eq. (13) and the linearized stiffness β_1 in Eq. (17), respectively. The initial parameter estimate for this control method is selected as:

$\hat{\theta}_S(0) + \beta_S(0) = \begin{bmatrix}120, & 0.1\end{bmatrix}^T$

The control gains in this control are chosen as same as before. Affected by the impulsive force, the vibration responses of X-shape structure system and SMD isolator under this adaptive control will be investigated in the following part. The displacement and velocity histories of the capture mechanism subjected to an impulse are shown in Figs. 15 and 14, respectively. No matter whether it is the X-shape structure system or the SMD isolator, mass m jumps up and down around the equilibrium point and stops after a period of time due to the existence of damping. The maximum displacements of mass m are 0.036 m and 0.035 m, which have same maximum velocity v = 0.101 m/s. It is seen that the curve of the X-shape structure system versus time histories is in agreement with that of the SMD isolator on the whole, which provides a good condition to do some comparison on the isolation performance of two vibration isolation systems.

After exerting the adaptive control into two systems, we can find these two vibration isolation systems are both effective when subjected to the external impulsive excitation according to Figs. 16 and 18. The maximums of x_X and x_S are 1.3×10^{-3} m and 2.0×10^{-4} m, respectively, which are relative small in comparison with the maximum one y_{max}. In addition, the X-shape isolation system has smaller vibration amplitude and needs

less time than the traditional SMD isolator to make the satellite platform keep stable. As depicted in Figs. 17 and 19, it means that the adaptive controller can ensure the asymptotic convergence of the tracking errors.

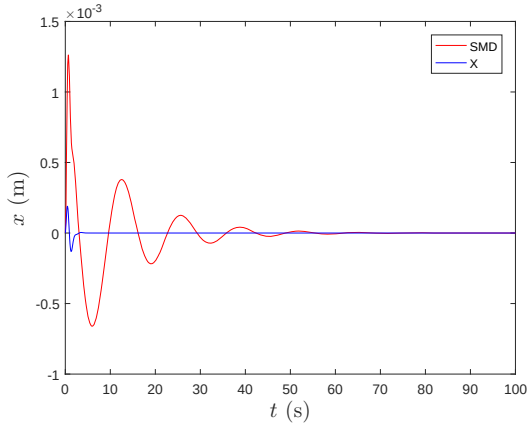

Figure 16: Displacement error of mass M for the X-shape structure and SMD isolators with control

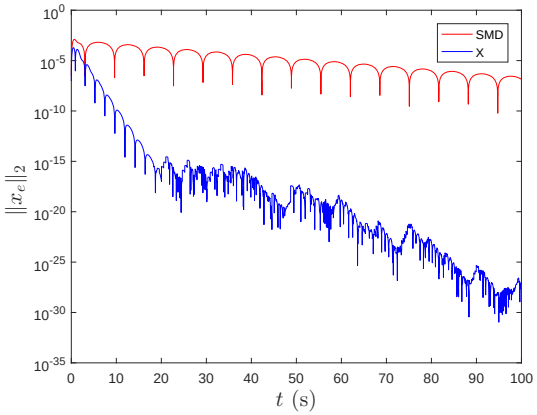

Figure 17: Displacement error norm of mass M for the X-shape structure and SMD isolators with control

Compared with the SMD isolator, the X-shape structure system has faster convergence rate and better vibration isolation performance. Fig. 20 shows that the observer error decays to zero approximately, which demonstrates that the velocity estimation $\hat{x}_2$ coincides with the practical velocity x_2. The control torque demands of the adaptive controller for two isolation systems are shown in Fig. 21. It is noted that the demands remain time-varying

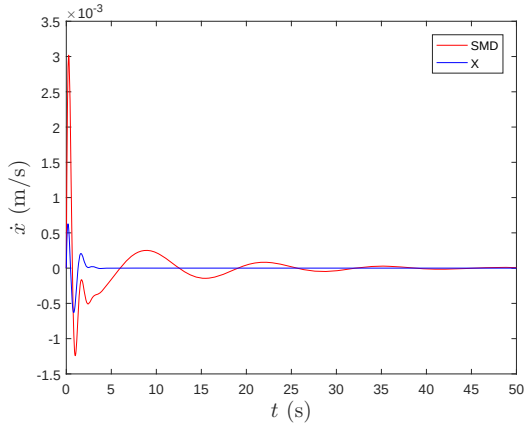

Figure 18: Velocity error of mass M for the X-shape structure and SMD isolators with control

and are close to zero ultimately. From Fig. 21, it is seen that the X-shape structure system acquires more initial control torque than SMD isolator. Fig. 22 provides the dynamic scaling factor r and indicates that it reaches a stable value at last and stops increasing when the observation error $\hat{x}_2 - x_2$ gets close to zero.

According to the results above, the X-shape structure system has a much better vibration isolation performance than the classical SMD isolator under the effect of an additional adaptive control when the structural parameters are unknown. Besides, the hybrid control strategy can make drifting motion disappear and provide a stable environment for the on-orbit spacecraft, which is vital to carry out the space missions successfully.

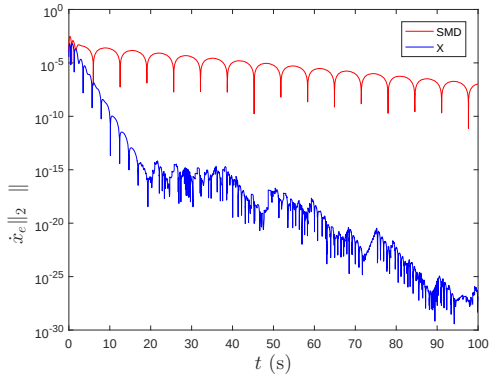

Figure 19: Velocity error norm of mass M for the X-shape structure and SMD isolators with control

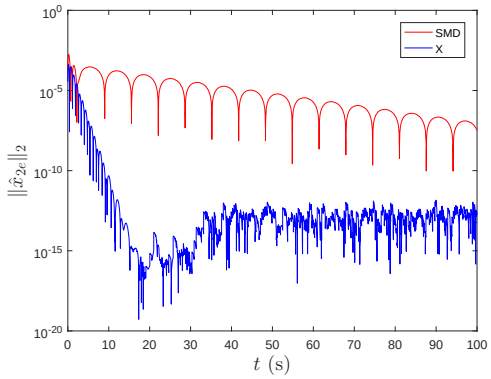

Figure 20: Velocity estimate error for the X-shape structure and SMD isolators with control

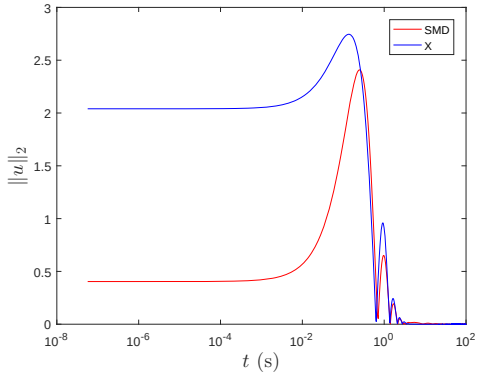

Figure 21: Control torque for the X-shape structure and SMD isolators with control

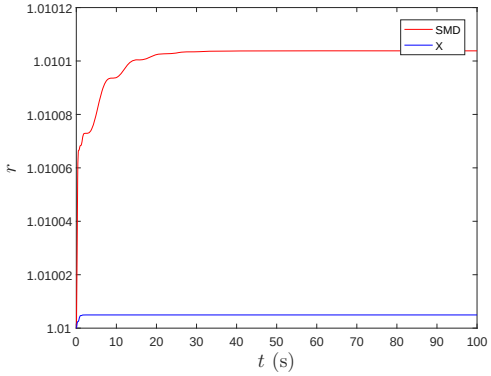

Figure 22: Scaling factor r for the X-shape structure and SMD isolators with control

5 Conclusion

In this paper, a hybrid passive/active controller of a loosely connected combined spacecraft system is proposed to suppress the post-capture vibrations of the combined system subjected to the impulsive external excitation. The X-shape structure is redesigned to achieve better stabilty of the whole system. A set of nonlinear ordinary differential equations that model the present combined system are established by Lagrange's principle and then solved directly by numerical integration method. In order to achieve better vibration isolation performance, an adaptive control method through dynamic scaling design is introduced to assist the X-shape vibration isolation system, considering that parameters M, c_1 and c_2 are all unknown. Besides, the asymptotic stability of the closed-loop system is verified in details. In numerical simulations, three cases are considered for comparison. Firstly, we compare the pure X-shape isolation system with uncontrolled SMD isolator and results demonstrate that the former one is better than the latter one by about five percent in terms of acceleration amplitude. The pure X-shape structure system has a better vibration isolation performance than the SMD isolator without active control. Secondly, influences of the active control method on isolation performance of the X-shape structure system are investigated. Numerical experiments show that it takes a short period of time to achieve stability for the X-shape structure system. Besides, the drifting problem emerged in the X-shape structure system is conquered, which ensures the whole spacecraft system stay stable quickly. Thirdly, compared with the typical SMD isolator with same control scheme, the X-shape structure system in conjunction with active control method obtains a much better isolation performance in all aspects, such as convergence rate, vibration amplitude, etc. In a word, the presently proposed hybrid passive/active control of the loosely connected combined system is very promising in the post-capture vibration suppression task in future space missions.

Conflicts of Interest: The authors declare that they have no conflicts of interest to report regarding the present study.

References

Abakumov, A.; Miatov, G. (2006): Control algorithms for active vibration isolation systems subject to random disturbances. *Journal of Sound and Vibration*, vol. 289, no. 4, pp. 889-907.

Badawy, A.; McInnes, C. R. (2008): On-orbit assembly using superquadric potential fields. *Journal of Guidance, Control, and Dynamics*, vol. 31, no. 1, pp. 30-43.

Bustan, D.; Sani, S. K. H.; Pariz, N. (2014): Retracted article: immersion and invariance based fault tolerant adaptive spacecraft attitude control. *International Journal of Control, Automation and Systems*, vol. 12, no. 2, pp. 333-339.

Clark, W. W. (2000): Vibration control with state-switched piezoelectric materials. *Journal of Intelligent Material Systems and Structures*, vol. 11, no. 4, pp. 263-271.

Dai, H.; Jing, X.; Sun, C.; Wang, Y.; Yue, X. (2018): Accurate modeling and analysis of a bio-inspired isolation system: with application to on-orbit capture. *Mechanical Systems and Signal Processing*, vol. 109, pp. 111-133.

Dai, H.; Jing, X.; Wang, Y.; Yue, X.; Yuan, J. (2018): Post-capture vibration suppression of spacecraft via a bio-inspired isolation system. *Mechanical Systems and Signal Processing*, vol. 105, pp. 214-240.

Karagiannis, D.; Sassano, M.; Astolfi, A. (2009): Dynamic scaling and observer design with application to adaptive control. *Automatica*, vol. 45, no. 12, pp. 2883-2889.

Lin, S. M. (2009): Vibration suppression of a moving beam subjected to an active-control electrostatic force. *Computer Modeling in Engineering and Sciences*, vol. 43, no. 1, pp. 73.

Liu, C.; Jing, X.; Chen, Z. (2016): Band stop vibration suppression using a passive X-shape structured lever-type isolation system. *Mechanical Systems and Signal Processing*, vol. 68, pp. 342-353.

Liu, C.; Jing, X.; Li, F. (2015): Vibration isolation using a hybrid lever-type isolation system with an X-shape supporting structure. *International Journal of Mechanical Sciences*, vol. 98, pp. 169-177.

Liu, X.; Ortega, R.; Su, H.; Chu, J. (2011): On adaptive control of nonlinearly parameterized nonlinear systems: towards a constructive procedure. *Systems & Control Letters*, vol. 60, no. 1, pp. 36-43.

Oh, H. U. (2004): Characteristics of a magneto-rheological fluid isolator obtained by permanent magnet arrangements. *Smart Materials and Structures*, vol. 13, no. 3, pp. N29-N35.

Park, W. (1967): Mass-spring-damper response to repetitive impact. *Journal of Engineering for Industry*, vol. 89, no. 4, pp. 587-596.

Saleh, J. H.; Lamassoure, E. S.; Hastings, D. E.; Newman, D. J. (2003): Flexibility and the value of on-orbit servicing: new customer-centric perspective. *Journal of Spacecraft and Rockets*, vol. 40, no. 2, pp. 279-291.

Seo, D.; Akella, M. R. (2008): High-performance spacecraft adaptive attitude-tracking control through attracting-manifold design. *Journal of Guidance, Control, and Dynamics*, vol. 31, no. 4, pp. 884-891.

Seo, D.; Akella, M. R. (2009): Non-certainty equivalent adaptive control for robot manipulator systems. *Systems & Control Letters*, vol. 58, no. 4, pp. 304-308.

Stoll, E.; Letschnik, J.; Walter, U.; Artigas, J.; Kremer, P. et al. (2009): On-orbit servicing. *IEEE Robotics & Automation Magazine*, vol. 16, no. 4, pp. 29-33.

Sun, X.; Jing, X. (2015): Multi-direction vibration isolation with quasi-zero stiffness by employing geometrical nonlinearity. *Mechanical Systems and Signal Processing*, vol. 62, pp. 149-163.

Sun, X.; Jing, X. (2016): A nonlinear vibration isolator achieving high-static-low-dynamic stiffness and tunable anti-resonance frequency band. *Mechanical Systems and Signal Processing*, vol. 80, pp. 166-188.

Vadiraja, D.; Sahasrabudhe, A. (2008): Vibration and control of rotating tapered thin-walled composite beam using macro fiber composite actuator. *Computer Modeling in Engineering and Sciences*, vol. 27, no. 1, pp. 49.

Wen, H.; Yue, X.; Li, P.; Yuan, J. (2017): Fast spacecraft adaptive attitude tracking control through immersion and invariance design. *Acta Astronautica*, vol. 139, pp. 77-84.

Wen, H.; Yue, X.; Yuan, J. (2017): Dynamic scaling-based noncertainty-equivalent adaptive spacecraft attitude tracking control. *Journal of Aerospace Engineering*, vol. 31, no. 2, 04017098.

Xavier, C.; Sun-Wook, K.; Michel, I.; Arun, M.; Gilbert, J. (1997): Post-impact dynamics of two multi-body systems attempting docking/berthing. *Acta Astronautica*, vol. 40, no. 11, pp. 759-769.

Yuan, Q.; Liu, Y.; Qi, N. (2017): Active vibration suppression for maneuvering spacecraft with high flexible appendages. *Acta Astronautica*, vol. 139, pp. 512-520.